International Journal of Impact Engineering 147 (2021) 103728

Contents lists available at ScienceDirect

International Journal of Impact Engineering

journal homepage: www.elsevier.com/locate/ijimpeng

Adiabatic heating and damage onset in a pultruded glass fiber reinforced composite under compressive loading at different strain rates.

Nazanin Pournoori*, Guilherme Corrêa Soares, Olli Orell, Sarianna Palola, Mikko Hokka, Mikko Kanerva

Engineering Materials Science, Faculty of Engineering and Natural Sciences, Tampere University, POB 33014, Tampere, Finland

ARTICLE INFO

Keywords:
Glass fiber-reinforced polymer composites
Adiabatic heating
Strain-rate effects
Compression

ABSTRACT

Damage onset and adiabatic heating of a pultruded Glass Fiber-Reinforced Plastic (GFRP) composite was investigated using compression tests at low, intermediate and high strain rates (10^{-3} s^{-1}, 1 s^{-1} and 10^{3} s^{-1}). Optical and infrared (IR) cameras monitored the specimens during testing, so that the mechanical response, damage onset, and damage evolution were obtained along with the adiabatic heating of the specimen due to plastic deformation and fracture. The results revealed clear strain rate effects on stiffness, strain softening and damage initiation. The simultaneous optical and IR imaging allowed quantitative description of thermo-mechanical response of the material and studying the formation and propagation of shear localizations and their temperature history. The maximum temperatures in the fracture zones exceed 80 °C at the strain rate of 10^{3} s^{-1}. Scanning Electron Microscopy (SEM) was used to identify the micro-scale crack paths at different strain rates. The findings allow more exact numerical predictions and design of tubular GFRP pipes for impact applications.

1. Introduction

Pipes, tubular beams and rebars are typically manufactured by pultrusion or pull-winding whenever fibrous composite materials are used. The use of long, continuous fibers allows for mechanical design of weight-efficiency and, finally, it results in lightweight components with a very high strength in the main fiber direction. Recently, pultruded fibrous beams and thin shells have attracted the interest of the industry of wireless networks due to the ability of these parts to pass on electromagnetic signals at extremely high frequencies [1,2]. Specialized lamp posts and runway sensor posts at airports have been manufactured of composites for long since their impact resistance can be accurately tailored and adjusted per application. The mechanical stiffness of the beams necessitates a high fraction of longitudinal fibers but leads to a low strength in the transverse direction [3,4]. In order to predict and modify impact damage onset in pultruded composite beams, the micromechanics must be understood for a range of strain rates in the thickness direction. For designing a structure, the damage models must be valid in terms of the failure onset and energy division into heat and plastic deformation [5–7]. In terms of fracture toughness in composites, it is not entirely clear how the strain rate affects the values and the crack tip plasticity – the quantification of the effect is challenging [8,9].

Recently, significant efforts have been carried out to characterize the high rate behavior of different fiber reinforced polymer (FRP) composites using the Split Hopkinson Pressure Bar (SHPB) [10–12]. However, the high strain rate behavior of FRP composites has not been fully established due to its dependence on the type of fiber and matrix, volume fraction of fibers as well as the fiber orientation. The comparison of glass and carbon fiber reinforced polymers (GFRP and CFRP respectively) under compressive loading have revealed that the impact resistance for both GFRP and CFRP reduces with an increase in strain rate, but CFRP has a lower impact resistance than GFRP at high strain rates (450 s^{-1}) [13]. Additionally, the dynamic compression of GFRP indicates that the high strain rate behavior of composite materials significantly depends on the fiber orientation [14,15]. These studies represented that the (averaged) ultimate stress of the unidirectional specimen for the fiber orientation of 0° with respect to loading axis increased about 100% compared to quasi-static results, and the main failure mode was tensile splitting along the fiber direction. However, the failure mode for the in-plane transverse compression of specimens with fiber orientations larger than 10° was dominated by fiber/matrix debonding with broken fibers as well. The effects of fiber volume fraction on ultimate strength was investigated at various strain rates for unidirectional GFRP and in-plane compressive loading, by El-Habak

* Corresponding author.
E-mail addresses: nazanin.pournoori@tuni.fi (N. Pournoori), guilherme.correasoares@tuni.fi (G. Corrêa Soares), olli.orell@tuni.fi (O. Orell), sarianna.palola@tuni.fi (S. Palola), mikko.hokka@tuni.fi (M. Hokka), mikko.kanerva@tuni.fi (M. Kanerva).

https://doi.org/10.1016/j.ijimpeng.2020.103728
Received 27 January 2020; Received in revised form 7 July 2020; Accepted 17 September 2020
Available online 01 October 2020

[16]. In the El-Habak's study, the ultimate stress increased slightly with increasing strain rate, which was in contrast to the results reported by Kumar et al. [15]. The compressive strength also increased with increasing fiber volume fraction at the high strain rate region (above 100 s^{-1}) [16].

The importance of strain rate on the gradual damage evolution in FRPs has received more attention recently; however, accurate failure characterization is still a challenge. Daniel et al. [17] investigated the new engineering failure criteria by testing and modeling of carbon/epoxy composite under multi-axial stress states at different strain rates (10^{-4}, 1 and 180–450 s^{-1}). Although the current failure theories serve as a reliable tool to evaluate the overall failure of materials under different strain rates, the full-field methods can be implemented to determine in-ply damage onset and heat generation. The high-speed imaging system is one of the most useful and accurate methods to monitor failure mechanisms of the deforming FRP for either transverse compression or in-plane shear loading [18,19].

Among the techniques to measure transient temperature during high rate compression tests, the embedded thermocouple (ETC) technique has been an appealing tool for investigations with polymers [20]. However, this method provides no simultaneous information on the damage mechanisms leading to the heat generation. In turn, high-speed infrared (IR) imaging can be used to measure transient temperature changes and their spatial distributions on a surface. Li et al. [21] studied the thermomechanical response of CFRP at a high rate (1000–3000 s^{-1}) using a high-speed infrared detector array, which demonstrated the temperature rise due to damage and damage rate sensitivity under both compression and tension loading. Recently, Tarfaoui et al. [22] investigated the heat dissipation versus damage evolution for a glass laminate composite under in-plane compressive loading. He found that the heat generation was dependent on the damage mode and the maximum temperature exceeded 219 °C during impact tests. These findings in the current literature suggest that simultaneous measurements of the damage mode, heat generation, and temperature could be functional to study also out-of-plane high rate loading and damage of FRPs with a high fiber volume fraction. Moreover, the measurements could be extended for a wider range of strain rates. In the current literature, the damage onset and adiabatic heating of high fiber volume fraction (pultruded) GFRP have not been solved for the important out-of-plane direction.

In this study, we pursue to understand the damage onset in pultruded high-performance GFRP under out-of-plane compressive loading at different strain rates. Out-of-plane impacts during operation of real structures are prone to result in damage that is challenging to predict for its propagation – especially for the transverse direction in the plane of the laminate. Here, three different strain rate regimes are considered and analyzed to establish the damage onset load level with the help of thermal measurements related to damage. SHPB device is applied to perform the tests at the highest rates ($\approx 10^3$ s^{-1}) and is coupled with the high-speed optical and IR cameras. Finally, DIC analysis is used to determine impact failure strains at strain rates from 10^{-3} s^{-1} to 10^3 s^{-1}. To gain detailed information on damage mechanism, the micro-failure analysis is carried out using SEM for the tested specimens.

2. Materials and methods

2.1. Specimen preparation and characterization

The material used in this work is a pultruded/pullwound laminate consisting of standard E-glass fiber roving (4800 tex, filaments with a $\approx$ 23 μm diameter, manufactured in Europe) embedded into polyester matrix (Norsodyne P 46074, Polynt, Bergamo, Italy). The laminate included three load-carrying layers of reinforcements with a stacking sequence of [0°, 85°, 0°]. The direction of 0° was set to match the long axis of the pultruded tubular laminate (Fig. 1). The thickness of the middle ply (85°) was 0.4 mm (4–8% of the specimen thickness). Cubic specimens were cut from the laminate using the wet-state Discotom-10 and Discotom-100 cut-off machines. All the cubic specimens were polished to minimize surface imperfections. Within polishing, the parallelism of the contact surfaces (to test machines) was controlled to be less than 0.1 mm and monitored using a 3D optical profilometer (InfiniteFocus G5, Alicona). The length of each side of a specimen was measured at least at five points and the average of these measurements was used for determining the individual dimensions. The specimens were compressed in out-of-plane direction that covered the ranges 10^{-3}, 1 and 10^3 s^{-1} (quasi-static, intermediate, high rate, respectively).

Stress distributions in a composite lay-up under mechanical loading are discontinuous and damage often initiates due to free-edge effects [23]. Therefore, for a constant lay-up, deviation in the stress gradients can affect the damage [16,24,25]. For the out-of-plane loading, the gradients can be varied by changing the cross-sectional size of the specimens. Here, the thickness of the specimens was 5.4 $\pm$ 0.2 mm, while the in-plane edge length was between 5 and 10 mm in different specimens. The specimen-corresponding stress during compression was computed using the exact specimen-specific cross-section dimensions.

The compression test specimens were analyzed after testing (quasi-static and intermediate strain rates) by using a scanning electron microscope Zeiss ULTRAplus (Zeiss, Germany). The specimens were encased on a SEM sample mold and embedded into molding epoxy (Epofix, Struers). For imaging, the SEM samples were polished and coated with carbon and gold to improve conductivity. The analysis was focused on defining the micro-scale failure modes in the composite specimens. The specimens, after high strain rate tests, were not characterized with a SEM (no integral specimen left).

A burn-off test was performed to determine the exact volume fraction of fibers in the GFRP laminate studied. Three samples were cut from the laminate with a planar size of one square inch (here 642 mm^2, average sample mass 7 gr) as is typical recommendation. Before testing, the samples were dried for 48 h at 50°C and then placed in a desiccator. For the burn-off, the samples were heated in two steps (heating ramp 60 min, first 0–280°C; second 280–565°C and hold for 60 min, free cool down) to burn off the matrix and leave the reinforcement. The fiber mass fraction was determined to be 74.4% (dry matter content). Furthermore, the fiber volume fraction was determined to be 54.8% using the mass fraction (W_f / W_{tot}) and densities as follows [26]:

$$V_f = \frac{1}{1 + (\rho_f/\rho_m)((W_{tot}/W_f) - 1)} \quad (1)$$

where W_{tot} is the total mass of the sample, and ρ_f= 2.58 gr/cm^3 is the density of the fiber and ρ_m = 1.08 gr/cm^3 is the density of the polyester matrix [27].

2.2. Quasi-static and intermediate strain rate tests

The quasi-static tests and the tests at intermediate strain rates were performed using an Instron 8800 servo-hydraulic universal testing machine with a 100 kN load cell. The cubic specimens were compressed between two rigid steel anvils at strain rates of approximately 10^{-3} and 1 s^{-1}. The applied load was recorded by a data acquisition system of the testing machine. An extensometer, as schematically shown in Fig. 2(a), was placed directly between the loading anvils adjacent to the specimen, which was synchronized with the testing machine to measure the strain (presuming anvils significantly stiffer). The quasi-static tests were also imaged using two 5 MPix (Elite) low-speed optical cameras, which were connected with the ADC converter to the testing machine for synchronizing the force data from Instron with the recorded deformation by the low-speed camera. Two Photron SA-X2 high-speed cameras and a Telops Fast IR M2k high-speed infrared camera were used to monitor the higher rate compression tests. Fig. 2(b) shows the experimental setup used for the intermediate strain rate tests.

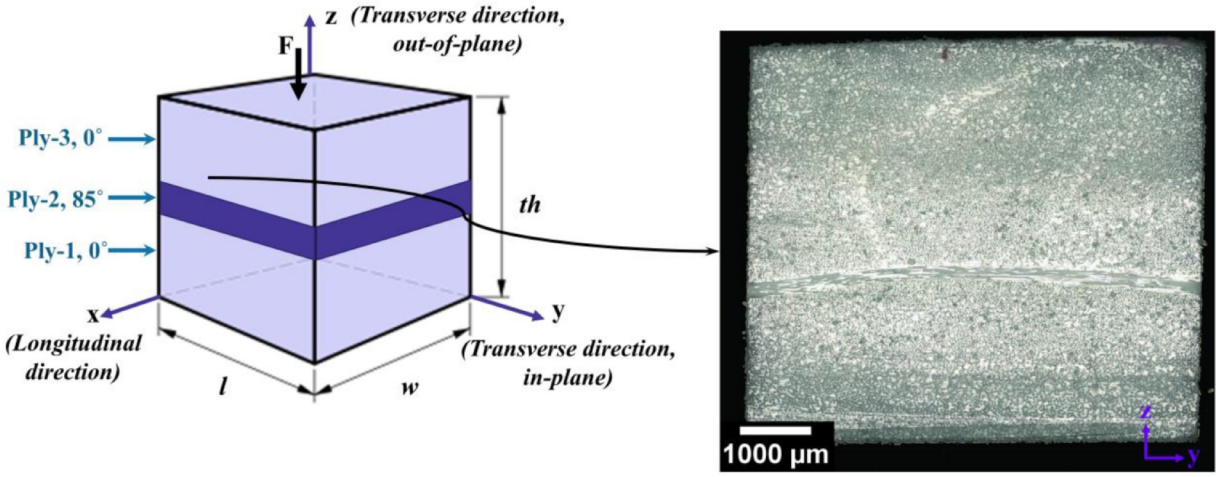

Fig. 1. (a) Schematic picture and (b) a microscope image of a test specimen.

2.3. High-strain rate tests

The high strain rate tests were carried out using a SHPB device. The SHPB setup consists of a striker, incident and transmitted bars (of aluminum). The aluminum alloy (6082-T6) bars were used here to better match the low mechanical impedance of the soft non-metallic GFRP specimens. The length of the striker bar used was 300 mm, and the total length of the incident and transmitted bars were 1800 mm with a 11.95 mm-diameter [28,29]. The schematic setup of the SHPB test is shown in Fig. 3. The specimen was sandwiched between incident and transmission bars with similar cross-sectional areas, and the bar ends were lubricated by a thin layer of vaseline to minimize the bar/specimen interface friction. Two strain gauges were attached on the incident and transmitted bars at the equal distance of 600 mm from the GFRP specimen to record the strain as a function of time [28]. A 0.1 mm-thick paper was used as a pulse shaper to generate a gentle compressive loading pulse. The pulse shaper also facilitates the dynamic stress equilibrium and almost constant strain rate deformation in the specimen. The impact of the striker, which was launched by compressed air in the gas gun, on the incident bar generates a desired compressive wave. When the compressive stress pulse reaches the incident bar/specimen interface, part of the incident pulse is reflected back as a wave of tension and part is transmitted through the specimen into the transmitted bar. The amplified strain gauge signals from the incident and transmitted bars were recorded on a high-speed digital oscilloscope, and the stress in the specimen were calculated from the dispersion-corrected strain gauge data. Based on the recorded strain history of the incident and transmitter bars, the engineering stress (σ_s) in the specimen can be obtained using one-dimensional wave-propagation theory as follows [30]:

$$\sigma_s = \frac{A_B}{A_s} E_B \varepsilon_T \tag{2}$$

Where ε_T is the transmitted waves, E_B and A_B are the Young's modulus and the cross-sectional areas of the bars and A_s is the initial cross-sectional area of the specimen. The strain for the high rate impact tests was measured from the full-field deformation images recorded by two high-speed cameras (see Section 2.2). The strain could be also obtained from the incident and reflected stress pulses, but better-quality results were obtained by measuring strain directly from the specimen.

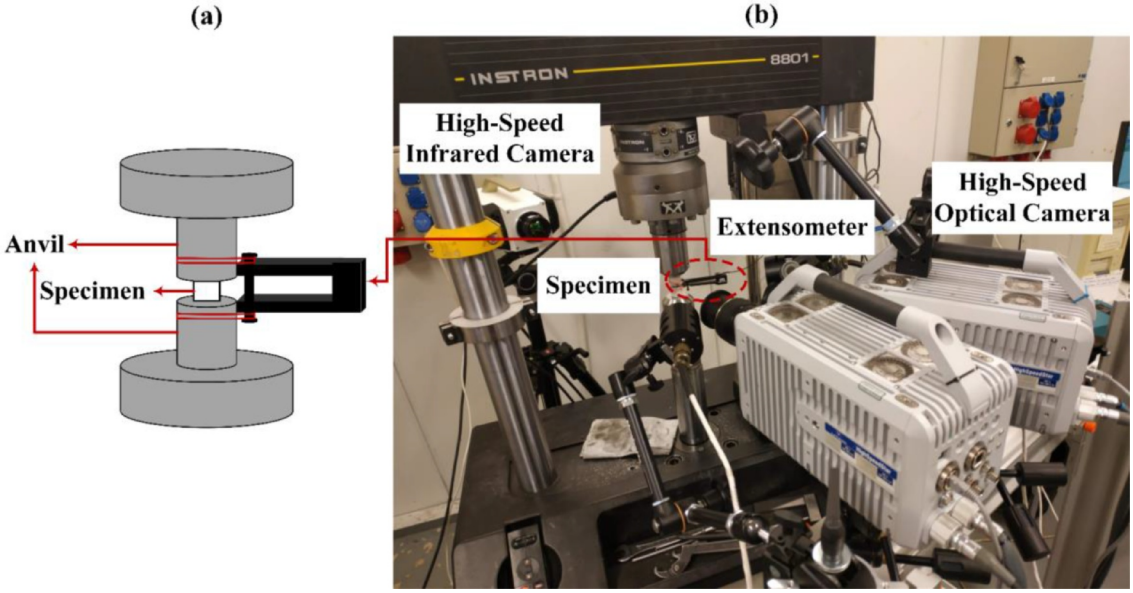

Fig. 2. (a) Schematic picture of the extensometer attached to the anvils of testing machine and (b) intermediate strain rate test setup with high-speed optical and infrared cameras used for in-situ monitoring of the experiment. (For interpretation of the references to color in this figure legend, the reader is referred to the web version of this article.)

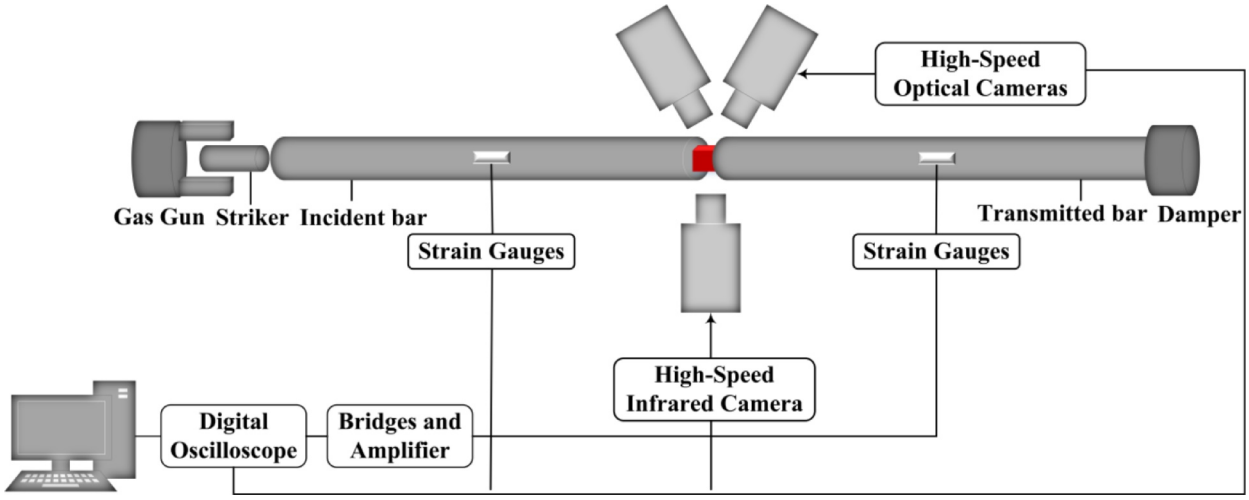

Fig. 3. Schematic picture of the compression SHPB setup with high-speed optical and infrared cameras used for in-situ monitoring of the experiments. (For interpretation of the references to color in this figure legend, the reader is referred to the web version of this article.)

During the high rate deformation, the full-field temperature of the specimen was also monitored using a high-speed infrared camera (see Section 2.2).

2.4. Strain and temperature full-field measurements

Full-field strain and temperature measurements were obtained using DIC and Infrared Thermography (IRT). The optical cameras were used to monitor the deformation of the patterned surface of the specimen, and digital image correlation was used to calculate the full-field displacement vector fields. High speed IRT was used to image the clean nonpattern side of the specimen and monitor the temperature rise during testing. As the camera systems were on opposite sides of a specimen, the IR images were mirrored so that the damage development (from opposite surfaces) matches on both DIC and IRT images.

The images of the quasi-static tests were recorded using two low-speed cameras with Nikon AF Micro-Nikkor 200 mm f/4D IF-ED lenses, while the intermediate and high rate tests were imaged by two high-speed cameras with Tokina AT-X PROD 100 mm f2.8 Macro lenses. Table 1 shows the frame rate, image resolution and image scale used in all investigated conditions for both optical and infrared systems. The displacement vectors were calculated from the images using Stereo-DIC with the DAVIS10 software suite from LaVision Inc. Here, the Stereo-DIC was preferred over 2D-DIC, as this setup functions better during the possible out-of-plane motion of the specimen, especially during the fracture of the specimen. Each specimen was loaded from the Z direction (out-of-plane direction), thus the full-field deformation on the surface of the specimens were recorded from either the Y-Z-plane (surface normal to the 0° fiber direction) or from the X-Z-plane (normal to the transverse laminate direction). The local surface strain fields were calculated with the DIC over the entire specimen surface. Then, the strain values, used in the force-strain curves, were obtained as the average of a region of interest using virtual gauges. Except for the images recorded from the X-Z-plane, the strain values after the appearance of the crack were determined using a virtual extensometer placed on the part of the specimen surface, which moves forward after the appearance of the crack. In this case the strain values were obtained by tracking the DIC displacements of two selected points, which were observable in the images of the specimen during the crack propagation. The spatial resolution of the computed strain field depends on at least the speckle pattern quality, Virtual Strain Gauge (VSG) size, and other DIC processing parameters. Therefore, the test specimens were prepared with a black speckle pattern on a fine layer of white paint, which was applied over the surface to prevent possible light reflections from the glass fibers. The VSG size and other DIC processing parameters are shown in Table 2. It is interesting to note that using different subset sizes (from 61 × 61 pixels to 19 × 19 pixels) for a set of pictures at strain rate of $10^3\ s^{-1}$ have no effect on strain measurements before the damage onset. In this study, the *damage onset* point was defined as the first timewise and visually observed crack in the recorded images of the specimen surface. However, the local strain fields during the damage evolution were obtained more precisely by applying smaller subset sizes (about 25 × 25 pixels).

The IR images were recorded using a Telops Fast-IR M2K high-speed infrared camera with a 50 mm lens during the high rate compression tests. For the intermediate strain rate tests, the infrared images were captured at 1 kHz frame rate with 100 μs exposure time, whereas the temperature was measured every 5 μs at 78 kHz frame rate during the high strain rate tests. It should be mentioned that the IR images recorded every 13 μs at high strain rate, while the optical images were recorded every 10 μs. Considering how fast the damage onset occurs in brittle materials, the 13 μs between the infrared frames can be somewhat long compared to the duration of the crack initiation. It would be desirable to use higher acquisition frequencies to improve the temporal matching between the temperature and force/strain data. However, the currently best available high-speed infrared imaging technology is maxed out at 90 kHz acquisition frequency with a very limited resolution (64 × 4 pixels). Despite the technical limitations, the imaging speed used in this work is the currently best available compromise between temporal and spatial resolutions.

Table 1
Frame rate, image resolution and image scale for optical and infrared cameras at different strain rates.

Strain rate (s^{-1})	Optical frame rate (Hz)	Optical image resolution (pix)	Optical image scale (pix/mm)	IR frame rate (Hz)	IR image resolution (pix)	IR image scale (pix/mm)
≈ $\mathbf{10^{-3}}$	2	1308 × 1144	100	–	–	–
1	10,000	512 × 304	39	1000	64 × 64	3
≈ $\mathbf{10^3}$	160,000	256 × 200	19	78,000	64 × 8	3

Table 2
DIC processing parameters.

Parameter	Strain rate $\approx 10^{-3}$ s^{-1}	1 s^{-1}	$\approx 10^{3}$ s^{-1}
Correlation method	Relative-to-first	Sum-of-differential	Sum-of-differential
Matching criteria	ZNSSD*	ZNSSD	ZNSSD
Subset size	99 pixels	49 pixels	25 pixels
Step size	33 pixels	16 pixels	8 pixels
Subset shape function	Affine	Affine	Affine
Interpolation method	6th Order spline function	6th Order spline function	6th Order spline function
Maximum stereo reconstruction error	0.65 pixel	1 pixel	1.5 pixel
VSG size	165 pixels	81 pixels	41 pixels

* ZNSSD: zero-normalized sum of squared differences.

The radiometric temperature measured by the IR camera assumes that the observed material has an emissivity of 1 and is a black body. A calibration curve to convert the radiometric temperature to true temperature was calculated considering that the applied IR Camera measures IR radiation with wavelengths from 1.5 to 5.4 μm and that the fiber reinforced plastic composites are known to have a directional spectral emissivity of approximately 0.9 for those wavelengths [31]. This calibration curve was calculated using the information from two different sources. First, the sample was imaged at room temperature while measuring its temperature with a K-type thermocouple. Second, a sample was painted with a thermographic paint with known emissivity, and slowly heating the sample on a hot plate. The radiometric temperature of the painted surface was converted into true surface temperature using its emissivity at a given temperature.

2.5. Stiffness determination

The stiffness of the composite specimen under compressive loading at various strain rates was determined using the slope of engineering stress-strain curve. For this purpose, the linear (least squares fit) regression was carried out to determine the slope of the estimated linear part of the data. The linear regime was estimated for the strain values between 0.005 to 0.015 (mm/mm). Average correlation of $AR^2 = 0.9977$ was achieved for the entire test matrix.

2.6. Finite element analysis

A finite element (FE) model was created using ABAQUS/Standard (2017) to indicate the stress state in the specimen due to compression and for the specific lay-up in this work. The model consisted of the 3D specimen model and the two steel (deformable) anvil models. The geometry of the specimen was created according to the real dimensions of the specimen used at the rate of 10^{-3} s^{-1}-test (see Fig. 6 for its behavior). A surface-to-surface contact formulation without friction was used for the interaction between the anvils and the specimen. The 3D brick element (C3D8) with the element size of 0.2 mm was used for discretizing. Boundary conditions were applied on each anvil model as shown in Fig. 4. A displacement restriction over all degrees of freedom was applied on the bottom surface of the lower anvil. The in-plane displacements were restricted at a middle point of the bottom surface of the GFRP to link it with the anvil. The translation at a middle point of the edge of the GFRP surface was also restricted in the direction parallel to the edge to finally prevent the free body motion. The in-plane displacement restrictions were applied also on the top surface of the upper anvil. Finally, a constant compressive displacement was applied on the upper anvil and the value was essentially equal to the displacement of the real specimen at the damage onset point of the test (0.19 mm). Each GFRP ply was modeled using engineering constants of $E_1 = 35$ GPa, $E_2 = 7$ GPa, $\nu_{12} = 0.3$, $\nu_{13} = 0.3$, $\nu_{23} = 0.3$, $G_{12} = 3.6$ GPa, $G_{13} = 2$ GPa, $G_{23} = 3.6$ GPa [32]. The modulus in the out-of-plane direction was fitted based on the measured force-displacement response and was $E_3 = 4.5$ GPa. This means that the three plies were presumed equal in terms of their linear-elastic behavior (in their local 123-coordinate system).

3. Results and discussion

3.1. Quasi-static and dynamic response of the composite

Each quasi-static and dynamic compression test (i.e., ranges 10^{-3}, 1 and 10^{3} s^{-1}) was repeated at least for two specimens at ambient laboratory conditions. It is important to note that the engineering stress over the cross-sectional area of the specimen does not represent the stress state in a composite specimen with a lay-up. Therefore, the compression data in terms of absolute (force) test data is important to report along with the normalized data (engineering stress).

Fig. 5 shows the simulated stress fields for the specimen under compression. The out-of-plane stress component (S_{33}) remarks the effects of the lay-up: the stress gradients at the ply interfaces are high and dependent on which side of the specimen is observed (the lay-up relation) and differ as much as 40%. For the in-plane stress components, even the sign of stress is different throughout the specimen.

Fig. 6 shows the measured force-strain response of the out-of-plane compression tests at the three different strain rate ranges. The strain used in Fig. 6 was the one obtained by using DIC. The comparison of the force-strain curves in general suggests the increase of stiffness (slope) for increasing strain rate due to the strain rate sensitivity – common in polymer composites due to the polymeric matrix phase. The detailed analysis of stiffness is in Section 3.2.3. In addition to the slope, the curve suggests the strain value at the maximum force. For the intermediate compression tests, it is less than that for the quasi-static (lowest rate) tests. The strain at the maximum force for the high rate tests was less than half of that of the intermediate rate tests, as shown in Table 3. The observed trend of an increasing slope and decreasing strain at the maximum force (peak) at the higher rates is presumed to be due to the viscoelasticity of the polyester matrix and fiber matrix interphases.

The shape of the quasi-static curves indicates non-linear elastic behavior especially when increasing the force prior to the maximum value. However, the force-strain curves of the intermediate and high rate tests are characterized by a very brief (in comparison to the quasi-static tests) non-linear regime prior to the peak force that, later, is followed by a drop and a significant increase in the specimen deformation (strain). This phenomenon may occur due to marked strain softening and adiabatic shear band localization. The localization will be discussed further in Section 3.3.

3.2. Evaluation of the mechanical damage and heat generation

The mechanical behavior of the specimens is evaluated at different strain rates to study the damage mechanism of the GFRP composite. Simultaneously, the temperature variation is illustrated to report the effects of damage initiation and damage evolution on the heat generation during the out-of-plane compression tests.

3.2.1. Compressive stress-strain behavior and adiabatic heat generation

In this section, the variation of engineering stress, strain and temperature under the intermediate and high strain rate tests are reported. Naturally, for the quasi-static test, as defined, the heat generation is not reported due to there being enough time for heat conduction through the material. The normalized intensity of load in the specimen, i.e. stress, is typically the variable in models of dissipation and heat generation. Here, the engineering stress (force divided by the specimen's cross-section area) is used as an unambiguous indicator of the entire specimen's stress level with the comparisons to thermal data. As shown in Fig. 5(b), the engineering stress represents the out-of-plane stress

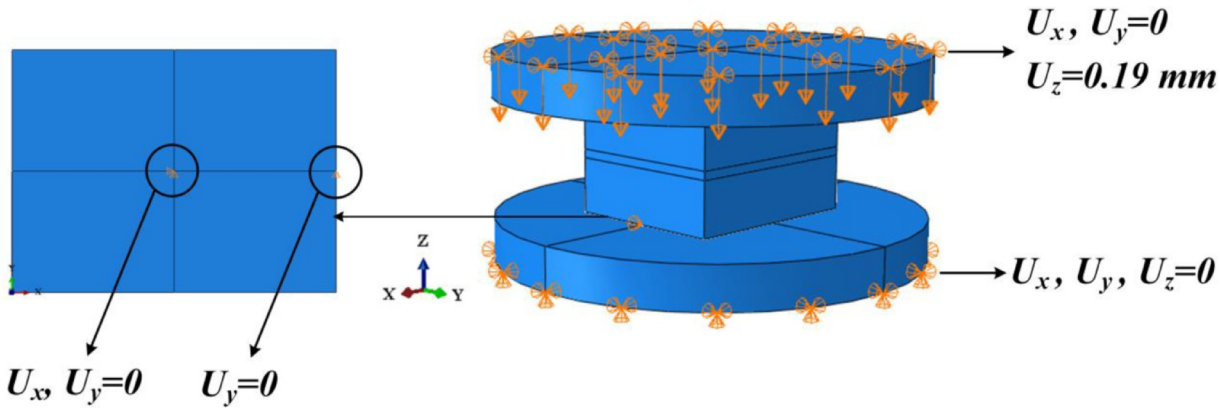

Fig. 4. Boundary condition and loading used for the finite element model and simulation of a quasi-static compression.

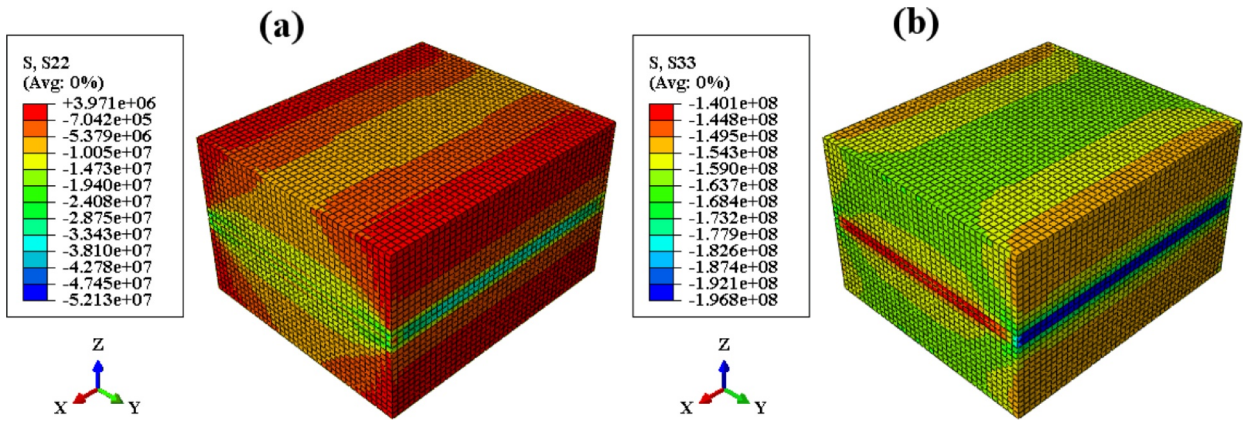

Fig. 5. Stress distribution in the GFRP specimen under quasi-static compression: (a) in-plane stress component S_{22} (local) and; (b) out-of-plane stress component S_{33} (local).

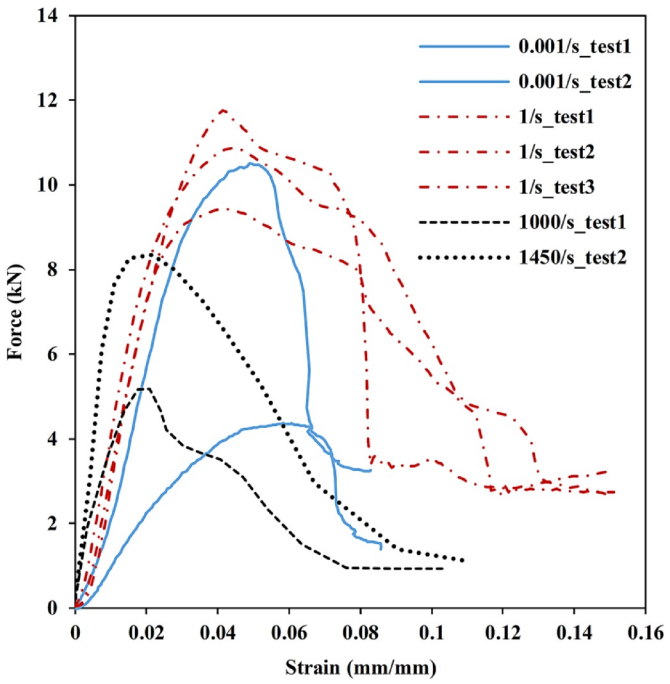

Fig. 6. Compressive, out-of-plane force-strain curves of the GFRP samples tested at various strain rates (Note: The code *_test i* refers to different test specimens).

Table 3
Maximum force and strain at maximum force at different strain rates.

Test rate	Maximum force (kN)	Strain at maximum force (mm/mm)
Low strain rate ($\approx 10^{-3}$ s^{-1})	10.5	0.049
	4.5	0.061
Intermediate strain rate (1 s^{-1})	9.5	0.042
	12	0.042
	11	0.044
High strain rate ($\approx 10^{3}$ s^{-1})	5	0.022
	8.5	0.021

level within a rather large volume and especially inside the specimen. The engineering stress and temperature as a function of strain at the strain rates of 1 and 10^3 s^{-1} are shown in Figs. 7(a) and (b). In these curves, the maximum temperature is the highest temperature observed in the specimen, and the reported temperature is the average temperature over the entire measured surface of the specimen.

In Fig. 7(a), the initial stress-strain curve shows a linear elastic behavior, and both the local maximum and the average temperatures do not change remarkably before the damage onset. The damage onset (i.e. first visually observed crack, indicated by 'D') appears within the yield point and also the maximum temperature starts increasing rapidly after this point. The maximum temperature continues to increase after the peak stress (approximately 13 °C maximum temperature increase) due to matrix cracking (see Section 3.3). After the point #3 in Fig. 7(a), the stress decreases abruptly because of the significant damage evolution. Since the crack has propagated through the specimen, the maximum temperature increases at the damaged zone and reaches ≈ 55 °C.

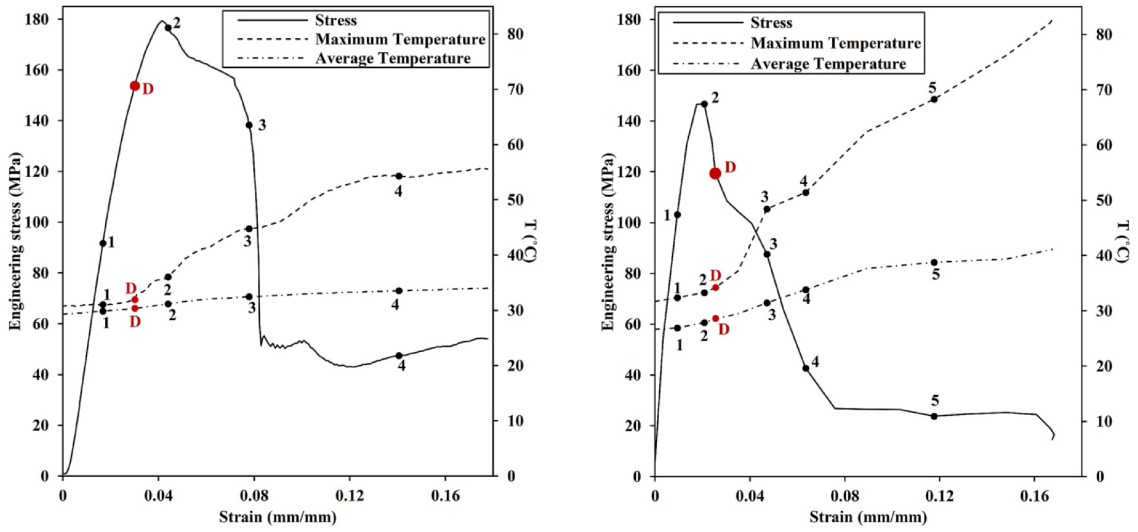

Fig. 7. Engineering stress and average and maximum temperatures as a function of strain at (a) intermediate strain rate (1 s^{-1}) and (b) high strain rate (≈ 10^3 s^{-1}). (Note: Numbers in each graph are related to the optical and thermal images shown in Fig. 8 and 9).

This heat generation is assumed to be, at least partly, caused by the energy released from the fiber-matrix debonding and friction due to micro scale sliding of the specimen fragments. The average temperature of the specimen surface does not change essentially during the intermediate rate compression, indicating that the heating is localized and the majority of the specimen's surface remains close to or at a room temperature.

Fig. 7(b) shows the engineering stress and average temperature of the specimen as a function of strain at the strain rate of ≈ 10^3 s^{-1}. At this strain rate, the damage onset (indicated by 'D') was observed visually from the recorded images after the peak of stress. Simultaneously, the local maximum temperature hardly increased (1 °C) during the linear stress-strain regime and up to the peak stress. However, the maximum temperature begins to dramatically increase after the damage onset and reaches 48 °C at the point #3. Therefore, the local maximum temperature of the specimen increases first due to the crack nucleation and matrix cracking and presumably fiber-matrix debonding. At the regime of the decreasing stress within the damage phase, also local fiber kinking might occur (see Section 3.3). From the point #3 to point #4, as indicated in Fig. 7(b), a slight increase in the average temperature (≈ 3 °C) can be observed and is related to the propagation of damage and cracking. Interestingly, after the point #4, the temperature increases while the nominal stress level continues to decrease, which might result from the fracture surface friction. During the testing at the strain rate of ≈ 10^3 s^{-1}, the maximum temperature of the specimen exceeded 80 °C, which corresponds to the observed catastrophic failure with matrix cracking, partial delamination of plies and interfacial (fiber-matrix) separation. Furthermore, the average specimen temperature continues to increase due to continuous nucleation of new damage sites and matrix plastic deformation throughout the specimen.

In summary, when comparing Fig. 7(a) and (b), it can be concluded that the anticipated damage mechanisms and especially the thermal response strongly depend on the strain rate. For the quasi-static and intermediate rate tests, the damage onset (visually observable crack) occurs close to the 'yield', i.e. end of the linear response and before the stress peak. Many works about the in-plane high rate compression have reported that the macroscopic damage onset occurs at or after the peak stress [16,33]. Fig. 7(b) indicates that the damage onset also appears after peak stress at the high strain rate (≈ 10^3 s^{-1}). This is suggested to be due to the major effects of the matrix when the specimen is compressed in the out-of-plane direction. It should be noted that the damage in terms of nonlinear (plastic) deformation in the test specimen can appear so that the force carrying-capability reduces prior to the damage onset defined here (a crack).

3.2.2. *Visualization of local damage and heat generation*

In this section, the optical monitoring of strain and temperature variation illustrates the localized damage and adiabatic heating profiles during the specimen deformation. Figs. 8 and 9 show the full-field

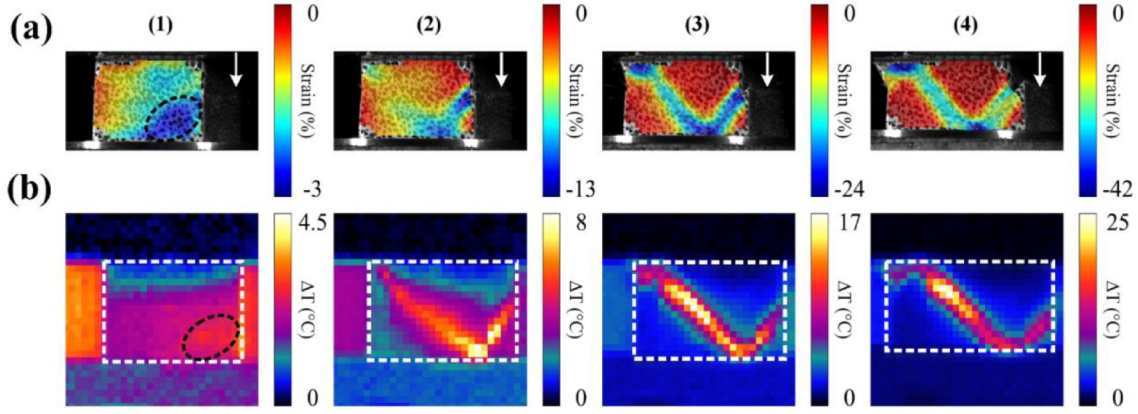

Fig. 8. (a) Full-field strain and (b) temperature maps for the composite under dynamic compressive loading at intermediate strain rate (1 s^{-1}). (Note: (1) The white arrows indicate the load direction. (2) The images in both (a) and (b) rows are sorted by the numbering in Fig. 7(a).).

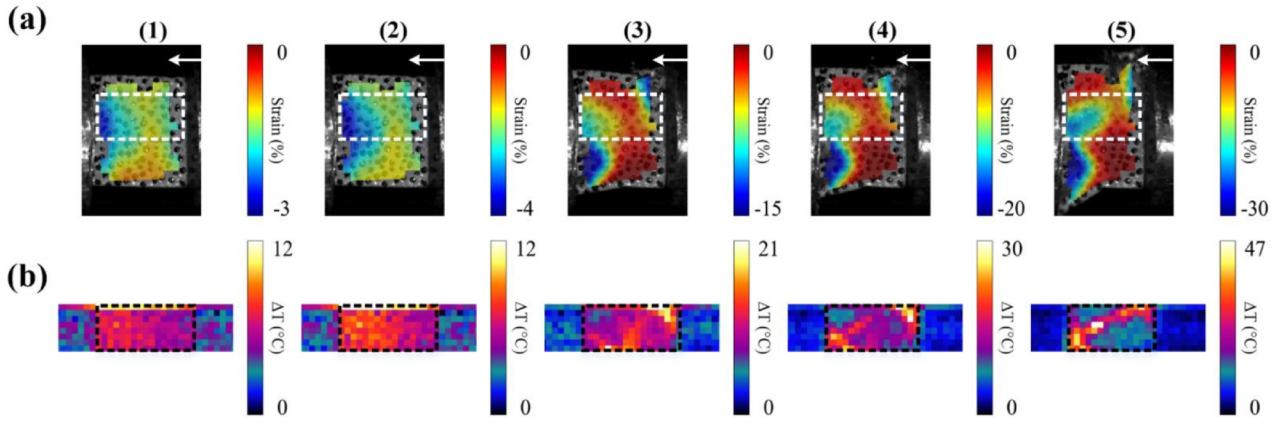

Fig. 9. (a) Full-field strain and (b) temperature maps for the composite under dynamic compressive loading at high strain rate ($\approx 10^3\ s^{-1}$). (Note: (1) The white arrows indicate the load direction. (2) The images in both (a) and (b) rows are sorted by the numbering in Fig. 7(b).).

strains and temperatures for strain rates of 1 and $10^3\ s^{-1}$. The numbering of the optical and infrared images shown in Figs. 8 and 9 correspond to the numbers indicated in Fig. 7. In Figs. 8 and 9, the scale bar changes to highlight the localized heat generation. The white arrows indicate the direction of compression.

The first images in Fig. 8(a) and (b) show the strain concentrations and related heat generation (highlighted by black contour). The strain concentrations are due to the appearance of microscopic surface damage in the specimen after the (compressive) contact with anvils. This behavior is obvious for the high rate tests before the damage onset in bulk specimen, as shown in Fig. 9(a) and (b) point #1 and #2 (compressive strain increases towards the other anvil).

Macroscopic cracks initiate due to the evolution of the microscopic damage as shown visually at point #2 in Fig. 8(a), and bottom left and top right corners of the specimen at point #4 in Fig. 9(a). It can be clearly seen that the macroscopic crack propagation prefers failure in shear, resulting in the V-letter shaped crack path for both intermediate and high rate tests. At the final failure phase, the specimen separates into pieces, as shown in the last right-side images in Figs. 8(a) and 9(a).

Similarly, as for the strain concentration, the heat generation occurs along the crack path, as exhibited by the V-letter shape in the temperature field. It should be mentioned that, in Fig. 9(b), the IR images do not cover the whole specimen surface, and only the part highlighted by the white contours was observed. Also, the area of the specimen outside the IR image has large strains, as shown in Fig. 9(a). As a result, more heat may have been accumulated in reality (as average over the surface), but unfortunately was not recorded in the images due to the low spatial resolution of the images and the system and the optical setup.

When comparing Figs. 8 and 9, it can be observed that more heat is generated in the high rate experiments compared to that generated at the intermediate rate tests. In addition, the damage generating the heat is distributed more homogeneously along the shear bands in the intermediate strain rate tests. The localized damage propagation observed in the high rate compression tests is believed to be affected by the thermal softening of the polymeric matrix amidst the shear bands.

3.2.3. Characterization of the damage onset

In this section, the detailed mechanics (modes) of damage are characterized. Fig. 10 summarizes the IR and optical data of the damage onset of visually observed cracks at different strain rates (1 and $10^3\ s^{-1}$). It should be noted that each image at a time show only one side (specimen surface) so that the crack nucleation could occur inside of the specimen or on the other surfaces as well.

For the intermediate strain rate test, a crack nucleates and starts to propagate at the interface of plies with different fiber orientation, as marked by the black circle contour in Fig. 10(a) and (c). In this case, the

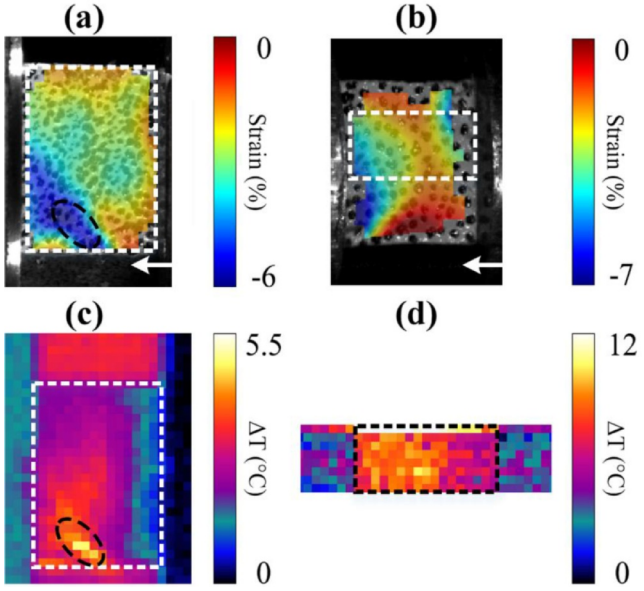

Fig. 10. (a) Full-field strain and (c) temperature maps for the damage onset point at intermediate strain rate ($\approx 1\ s^{-1}$). (b) Full-field strain and (d) temperature maps for the damage onset point at high strain rate ($\approx 10^3\ s^{-1}$). (Note: (1) The white arrows indicate the load direction. (2) the images are related to the 'D' point in Fig. 7(a) and (b).).

cracking propagates diagonally towards the free surface and forms a V-shaped shear band. In turn, Fig. 10(b) demonstrates the very beginning of the crack nucleation in the high rate test at the two opposite corners of the specimen, bottom left and top right corners. These cracks propagate diagonally through the specimen leading to the V-shaped path (Fig. 9, points #4 and #5). However, heat generation (a concentration) in the crack nucleation zone could not be seen in Fig. 10(d) as the IR images were recorded only over a part of the surface.

Table 4 presents the engineering stress levels and the average strains related to the visually observed damage onset for different strain rate tests. The strain at the damage onset in the low and intermediate rate tests were measured using both DIC and extensometer. It is apparent that the DIC results are in a good agreement with the results obtained from the extensometer measurements. The stress-strain slopes (stiffness) were also calculated for the quasi-static and intermediate rate compression tests and are presented in Table 4.

Table 4
Stiffness and the defined damage onset point of GFRP per strain rate range.

Test rate	Damage onset strain (mm/mm)	Damage onset engineering stress (MPa)	Damage onset force (kN)	Slope (estimated modulus) (GPa)
Low strain rate range ($\approx 10^{-3} s^{-1}$)	0.05 (0.035, DIC)	140	9.5	4.4
	0.055 (0.05, DIC)	135	4.2	4.5
Intermediate strain rate range (1 s^{-1})	0.025 (0.025, DIC)	165	8.5	9.3
	0.03 (0.03, DIC)	150	10	6.7
	0.04 (0.04, DIC)	208	10.8	9.2
High strain rate range ($\approx 10^{-3} s^{-1}$)	0.035, DIC	130	7.2	N/A
	0.025, DIC	120	4.2	N/A

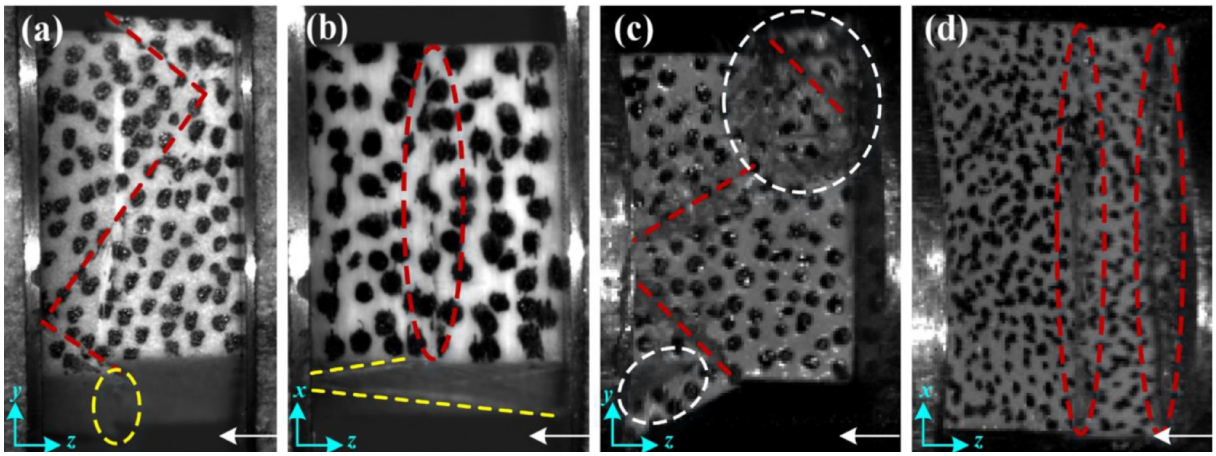

Fig. 11. High-speed images and highlighted shape of the damage. The images were obtained from two different in-plane directions at a low strain rate $\approx 10^{-3}\ s^{-1}$ (a)-(b); and at high strain rate $\approx 10^{3}\ s^{-1}$ (c)-(d). The white arrows indicate the compression direction.

3.3. Post-test modes of micro-scale failure

The microscopic failure mechanism was characterized by studying the specimens with the optical cameras during deformation and by a post-failure analysis using the scanning electron microscopy (SEM). The analysis is important to understand the distinct failure modes, i.e. matrix, interface and fiber failure modes in GFRP. Fig. 11 shows optical photographs of the specimen obtained after decreasing the stress level and complete unloading. The photographs were obtained from two different perpendicular directions from different specimens to study the different sides relative to the lay-up. Figs. 11(a) and (c) show that the crack forms a V-letter shape on the surface (Y-Z-plane) normal to the dominating longitudinal (0°) fiber direction for both low and high rate tests. The cracks mainly propagate under shear load and the crack-front (plane) parallel to the fibers. In turn, as shown in Figs. 11(b) and (d), the observed damage zone is parallel to the fiber direction on the surface (X-Z-plane) normal to the transverse laminate direction.

Figs. 12 show the SEM images of a specimen tested at the strain rate of $10^{-3}\ s^{-1}$. The damage initiation point is presumed (stress concentrations at Fig. 5) at the interface of different plies and revealed by matrix cracks as highlighted by the red contour in Fig. 12(b). The crack propagated diagonally, similarly as the two other indicated cracks, which have propagated through the matrix and fiber-matrix interfaces, as shown in Fig. 12(c) and (e). It can be also observed in Figs. 12(d) and (e) that slight fiber kinking might occur due to stiffness (and respective deformation) changes between the plies, as emphasized by the yellow contour.

Figs. 13 and 14 depict the sequence of failure in the specimen due to the intermediate strain rate compression. The damage initiation (see Fig. 7(a), point 'D') is clearly shown at the interface of the plies as highlighted by location #1 in red color in Figs. 13(a) and (b). Furthermore, another crack appears on the opposite inferior corner, as shown in location #2 in Fig. 13(b) that might be a result of the geometric imperfections of the specimen. The crack propagation through the specimen towards the free edge and contact surface is marked by number #3 in red color in Figs. 13(d) and (e).

The damage evolution at the strain rate of $1\ s^{-1}$ involves initiation of many cracks observed in the specimen after testing. Fig. 14 shows SEM images of the specimen after the experiment. Several half-millimeter to millimeter-long cracks, as shown by green contours, are illustrated in Fig. 14(c) and (d). Interestingly, Fig. 14(d) and (f) reveal fiber-breakage in the longitudinal direction of fibers that is unexpected for the dominating shear failure. This fiber shattering could be found in several locations of the specimen and is related only to the $1\ s^{-1}$ rate test – it is anticipated to occur also at the strain rate of $10^{3}\ s^{-1}$. This shattering does not (only) break the fibers into shorter segments but drives multiple cracks in the radial direction. This means clearly larger fracture surfaces than only the smallish fiber cross-section. The fiber breakage can be a significant feature affecting the heat generation and crack path division at higher rates. The strain rate sensitivity of fibers has been studied but is typically related to the longitudinal direction of fibers [34]. Glass and especially carbon fibers have a complex internal structure that incurs anisotropy in terms of stiffness, thermal expansion, and failure. Naturally, significant release of energy due to fiber cracking over large surfaces suggest heat generation as well as following strain softening due to the immediate local stress transfer between fibers and matrix. What is essential, from the point of view of the macro structure's design, is that the neighboring meso-scale failure modes are similar (i.e. dominating shear failure) between the different rates in the tests presented here. In future, correct connections between micro and meso-scale failure modes predicted by numerical failure criteria must be verified for the out-of-plane compression.

5. Conclusions

This study investigated the adiabatic heat generation and failure

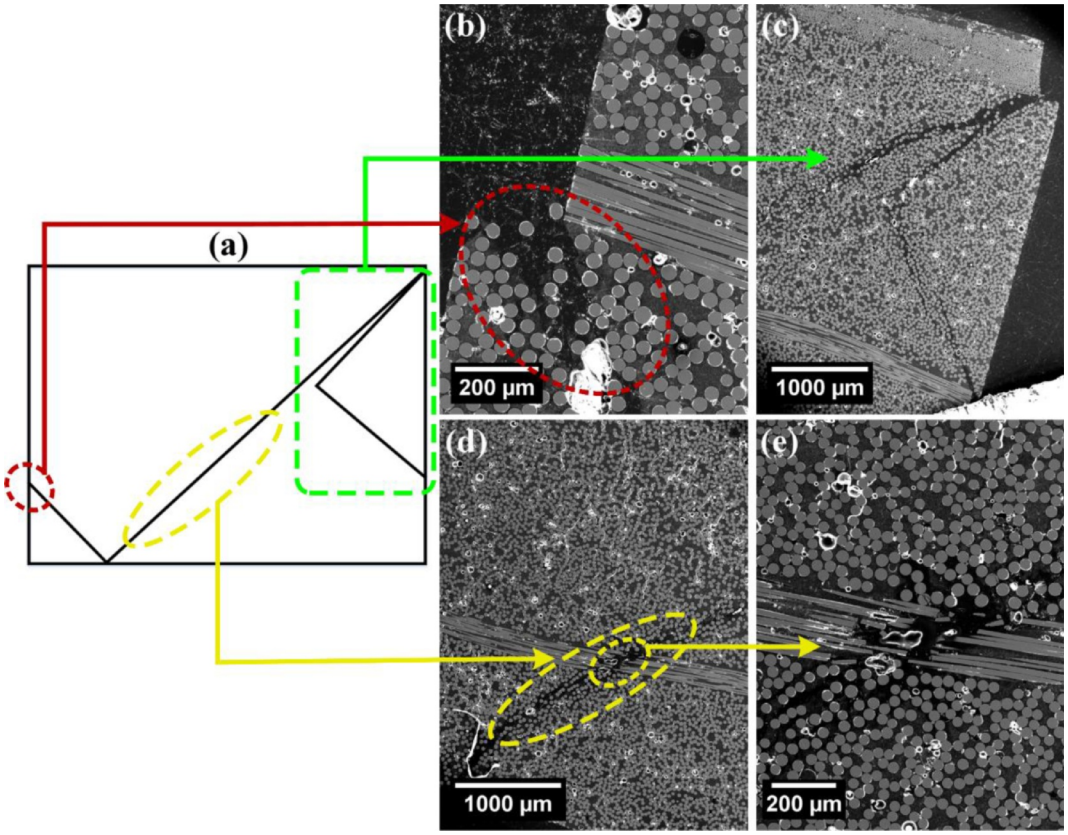

Fig. 12. SEM image of the specimen deformed at the strain rate of 10^{-3} s^{-1} (a) a schematic picture of the damaged specimen (b) damage onset zone, (c) matrix crack, (d) crack growth through different plies, and (e) matrix-fiber debonding.

onset in pultruded GFRP during dynamic compression at a wide range of strain rates from 10^{-3} to 10^{3} s^{-1}. Here, we focused on the thermal behavior and its relation to the onset of mechanical damage for out-plane loading (z-direction). The results obtained in this study can be summarized as follows:

- An increase in stiffness (≈90%) and a decrease in strain at the maximum compressive force was observed with increasing strain rate from quasi static to intermediate strain rate – affecting any design of tubular GFRP parts for high rate loadings.
- The temperature rise is mainly due to the meso-scale (in-ply) damage onset and crack propagation. The local maximum temperature at cracks significantly increases already in the early stages of loading, due to rapid damage propagation under adiabatic conditions, for the high rate compression.
- The dominating bulk failure mode, as can be seen in both thermal and strain profiles, occurs under shear leading to a V-shape form of localization and final crack path.
- For the 10^{-3} and 1 s^{-1} strain rate tests, the visually observed damage onset occurs after the non-linearity point of the anisotropic GFRP specimen and the damage initiates at the interface between the different plies with different orientation. Whereas, the damage onset at the strain rate of 10^{3} s^{-1} appears after the peak load (engineering stress) and the damage initiates near the contact surfaces.
- The micro-scale failure mode depends on the strain rate. For the tests carried out at the strain rate of 1 s^{-1}, fiber shattering as multiple radial cracks per fiber occurs in addition to the common matrix and interface failure, while this failure mode has not been

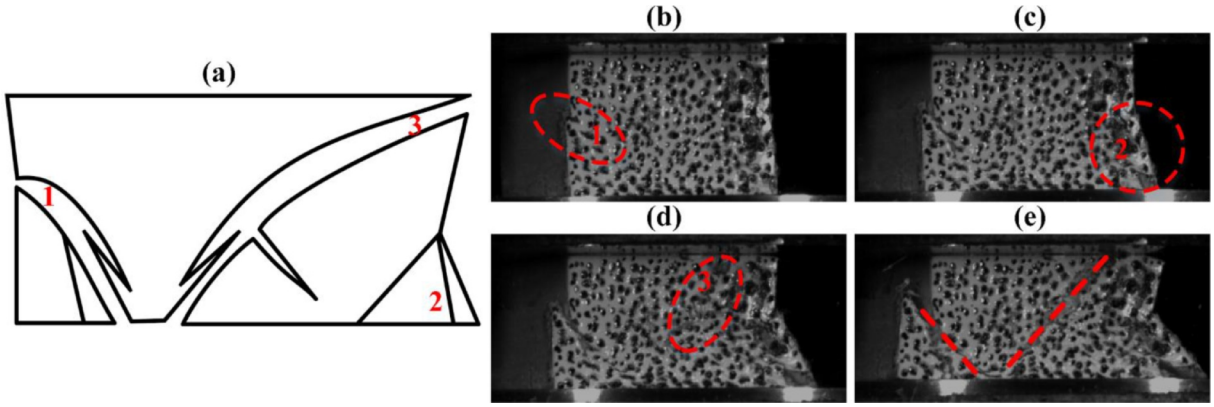

Fig. 13. Optical image sequence of a specimen deformed at the strain rate of 1 s^{-1} where crack initiation and propagation can be observed (a) schematic picture of the deformed specimen, (b) damage onset, (c) appearance of the second crack, (d) crack propagation diagonally, and (e) the formation of the V-shape crack.

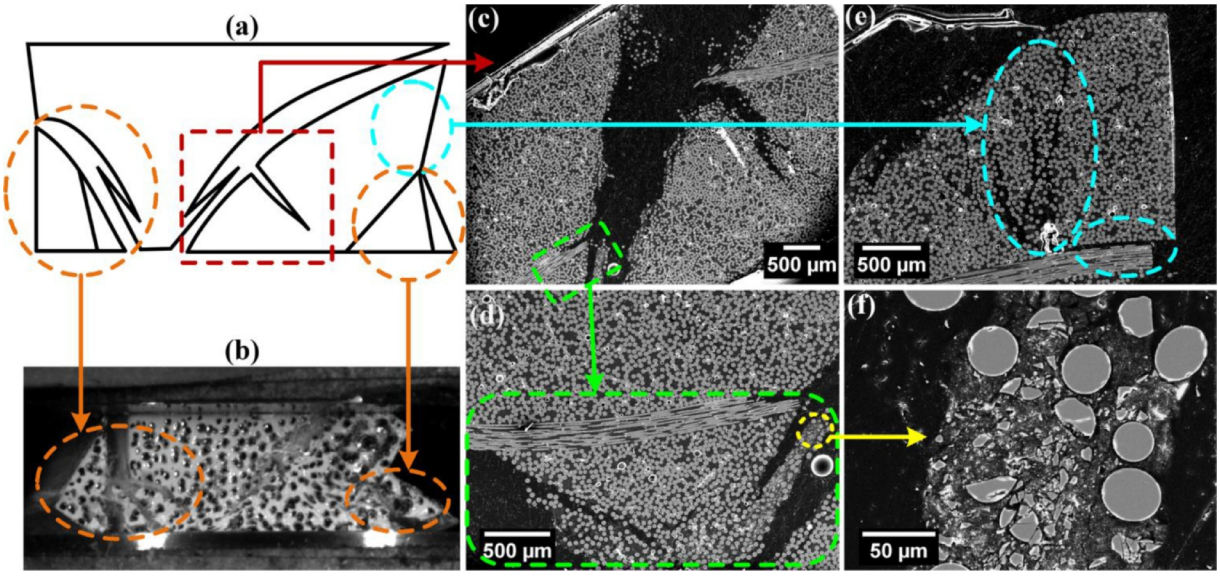

Fig. 14. SEM and optical images of the damaged zone of a specimen deformed at the strain rate of 1 s^{-1} (a) schematic image of the damaged specimen, (b) an optical image of the damaged specimen with localized shear bands, (c) cracked specimen with different damage modes, (d) matrix crack and matrix-fiber debonding, (e) shearing and delamination, and (f) fiber breakage.

observed at the rate of 10^{-3} s^{-1}.

Funding

Business Finland, Luxturrim5G subtask (10098/31/2016), Tampere University.

CRediT authorship contribution statement

Nazanin Pournoori: Formal analysis, Investigation, Software, Validation, Visualization, Writing - original draft. **Guilherme Corrêa Soares:** Formal analysis, Investigation, Writing - review & editing. **Olli Orell:** Formal analysis, Investigation. **Sarianna Palola:** Investigation. **Mikko Hokka:** Conceptualization, Methodology, Supervision, Writing - review & editing. **Mikko Kanerva:** Funding acquisition, Project administration, Software, Supervision, Writing - review & editing.

Declaration of Competing Interest

Authors declare and are aware of no conflicts of interest related to this work.

Acknowledgments

This study was funded by a grant from Business Finland related to the 'LuxTurrim5G' project and the related subtask (10098/31/2016) carried out by Tampere University of Technology and also by a grant from Tampere University. This work made use of Tampere Microscopy Center facilities at Tampere University.

Supplementary materials

Supplementary material associated with this article can be found, in the online version, at doi:10.1016/j.ijimpeng.2020.103728.

References

[1] Kanerva M, Lassila M, Gustafsson R, O'shea G, Aarikka-Stenroos L, Hemilä J. Emerging 5 G technologies affecting markets of composite materials. Exel White paper EWVL1:1:2018-1. Excel Composites; 2018 (accessed October 7.2020). https://www.luxturrim5g.com/publications.

[2] Characterization of mmWave Radomes for Base Stations and Automotive Radars - IEEE Conference Publication n.d. https://ieeexplore.ieee.org/document/8739914 (accessed November 18, 2019).

[3] Li Z, Khennane A, Hazell PJ, Brown AD. Impact behavior of pultruded GFRP composites under low-velocity impact loading. Compos Struct 2017;168:360–71. https://doi.org/10.1016/j.compstruct.2017.02.073.

[4] Di Vito D, Pärnänen T, Jokinen J, Orell O, Kanerva M. Lateral indentation and impact analyses on curved composite shells. Lect. Notes Mech. Eng.. Pleiades Publishing; 2019. p. 171–83. https://doi.org/10.1007/978-981-13-0411-8_17.

[5] Mulliken AD, Boyce MC. Mechanics of the rate-dependent elastic-plastic deformation of glassy polymers from low to high strain rates. Int J Solids Struct 2006;43:1331–56. https://doi.org/10.1016/j.ijsolstr.2005.04.016.

[6] Kanters MJW, van Erp TB, van Drongelen M, Engels TAP, Govaert LE. Loading rate dependence of failure strength as predictor for the long-term performance of thermoplastic polymeric products. Polym Test 2017;59:177–84. https://doi.org/10.1016/j.polymertesting.2017.01.026.

[7] Siviour CR, Jordan JL. High strain rate mechanics of polymers: a review. J Dyn Behav Mater 2016;2:15–32. https://doi.org/10.1007/s40870-016-0052-8.

[8] May M. Measuring the rate-dependent mode I fracture toughness of composites - A review. Compos Part A Appl Sci Manuf 2016;81:1–12. https://doi.org/10.1016/j.compositesa.2015.10.033.

[9] Asprone D., Cadoni E., Prota A., Manfredi G. Strain-rate sensitivity of a pultruded E-glass/polyester composite n.d. 10.1061/ASCECC.1943-5614.0000036.

[10] Griffiths LJ, Martin DJ. A study of the dynamic behaviour of a carbon-fibre composite using the split Hopkinson pressure bar. J Phys D Appl Phys 1974;7:2329–41. https://doi.org/10.1088/0022-3727/7/17/308.

[11] Ploeckl M, Kuhn P, Grosser J, Wolfahrt M, Koerber H. A dynamic test methodology for analyzing the strain-rate effect on the longitudinal compressive behavior of fiber-reinforced composites. Compos Struct 2017;180:429–38. https://doi.org/10.1016/j.compstruct.2017.08.048.

[12] Acharya S, Mondal DK, Ghosh KS, Mukhopadhyay AK. Mechanical behaviour of glass fibre reinforced composite at varying strain rates. Mater Res Express 2017;4. https://doi.org/10.1088/2053-1591/aa63dc.

[13] Ochola RO, Marcus K, Nurick GN, Franz T. Mechanical behaviour of glass and carbon fibre reinforced composites at varying strain rates. Compos Struct 2004;63:455–67. https://doi.org/10.1016/S0263-8223(03)00194-6.

[14] Tarfaoui M, Choukri S, Neme A. Effect of fibre orientation on mechanical properties of the laminated polymer composites subjected to out-of-plane high strain rate compressive loadings. Compos Sci Technol 2008;68:477–85. https://doi.org/10.1016/j.compscitech.2007.06.014.

[15] Kumar P, Garg A, Agarwal BD. Dynamic compressive behaviour of unidirectional GFRP for various fibre orientations. Mater Lett 1986;4:111–6. https://doi.org/10.1016/0167-577X(86)90061-3.

[16] El-habak AMA. Compressive resistance of unidirectional GFRP under high rate of loading. J Compos Technol Res 1993;15:311–7. https://doi.org/10.1520/ctr10384j.

[17] Daniel IM, Werner BT, Fenner JS. Strain-rate-dependent failure criteria for composites. Compos Sci Technol 2011;71:357–64. https://doi.org/10.1016/j.compscitech.2010.11.028.

[18] Okereke MI, Paul Buckley C, Akpoyomare AI. The mechanism of rate-dependent off-axis compression of a low fibre volume fraction thermoplastic matrix composite. Compos Struct 2017;168:685–97. https://doi.org/10.1016/j.compstruct.2017.02.070.

[19] Koerber H, Xavier J, Camanho PP. High strain rate characterisation of unidirectional carbon-epoxy IM7-8552 in transverse compression and in-plane shear using digital image correlation. Mech Mater 2010;42:1004–19. https://doi.org/10.1016/j.mechmat.2010.09.003.
[20] Rittel D. Transient temperature measurement using embedded thermocouples. Exp Mech 1998;38:73–8. https://doi.org/10.1007/BF02321647.
[21] Li Z, Lambros J. Dynamic thermomechanical behavior of fiber reinforced composites. Compos Part A Appl Sci Manuf 2000;31:537–47. https://doi.org/10.1016/S1359-835X(99)00102-5.
[22] Tarfaoui M, El Moumen A, Ben Yahia H. Damage detection versus heat dissipation in E-glass/Epoxy laminated composites under dynamic compression at high strain rate. Compos Struct 2018;186:50–61. https://doi.org/10.1016/j.compstruct.2017.11.083.
[23] Mittelstedt C, Becker W. Free-edge effects in composite laminates. Appl Mech Rev 2007;60:217–45. https://doi.org/10.1115/1.2777169.
[24] Salvi AG, Waas AM, Caliskan A. Specimen size effects in the off-axis compression test of unidirectional carbon fiber tow composites. Compos Sci Technol 2004;64:83–97. https://doi.org/10.1016/S0266-3538(03)00214-8.
[25] Bing Q, Sun CT. Specimen size effect in off-axis compression tests of fiber composites. Compos Part B Eng 2008;39:20–6. https://doi.org/10.1016/j.compositesb.2007.02.010.
[26] Kanerva M, Jokinen J, Sarlin E, Pärnänen T, Lindgren M, Järventausta M, et al. Lower stiffness of GFRP after sulfuric acid-solution aging is due to degradation of fibre-matrix interfaces? Compos Struct 2019;212:524–34. https://doi.org/10.1016/j.compstruct.2019.01.006.
[27] NORSODYNE® P 46074. Technical data sheet. Polynt Composites 2016.
[28] Vuoristo T, Kuokkala VT. Creep, recovery and high strain rate response of soft roll cover materials. Mech Mater 2002;34:493–504. https://doi.org/10.1016/S0167-6636(02)00177-1.
[29] Vuoristo T., Kuokkala V.-.T. Effect of Strain Rate, Moisture and Temperature on the Deformation Behavior of Polymer Roll Covers n.d. 10.1177/0014485104042949.
[30] Hopkinson Split. Chen Weinong W, editor. (Kolsky) Bar - Design, Testing and Applications, 18. Springer; 2019 n.d https://www.springer.com/gp/book/9781441979810 accessed November.
[31] Adibekyan A, Kononogova E, Monte C, Hollandt J. Review of PTB measurements on emissivity, reflectivity and transmissivity of semitransparent fiber-reinforced plastic composites. Int J Thermophys 2019;40. https://doi.org/10.1007/s10765-019-2498-0.
[32] Garcia OR. Master Thesis. Tampere University of Technology; 2018.
[33] Arbaoui J, Tarfaoui M, El Malki Alaoui A. Mechanical behavior and damage kinetics of woven E-glass/vinylester laminate composites under high strain rate dynamic compressive loading: experimental and numerical investigation. Int J Impact Eng 2016;87:44–54. https://doi.org/10.1016/j.ijimpeng.2015.06.026.
[34] Davies GAO, Olsson R. Impact on composite structures. Aeronaut J 2004;108:541–63. https://doi.org/10.1017/S0001924000000385.